Wafer-Scale Graphene Integrated Circuit
Yu-Ming Lin, *et al.*
Science **332**, 1294 (2011);
DOI: 10.1126/science.1204428

This copy is for your personal, non-commercial use only.

If you wish to distribute this article to others, you can order high-quality copies for your colleagues, clients, or customers by clicking here.

Permission to republish or repurpose articles or portions of articles can be obtained by following the guidelines here.

The following resources related to this article are available online at www.sciencemag.org (this infomation is current as of June 16, 2011):

Updated information and services, including high-resolution figures, can be found in the online version of this article at:
http://www.sciencemag.org/content/332/6035/1294.full.html

Supporting Online Material can be found at:
http://www.sciencemag.org/content/suppl/2011/06/08/332.6035.1294.DC1.html

This article **cites 23 articles**, 2 of which can be accessed free:
http://www.sciencemag.org/content/332/6035/1294.full.html#ref-list-1

This article appears in the following **subject collections:**
Physics, Applied
http://www.sciencemag.org/cgi/collection/app_physics

Downloaded from www.sciencemag.org on June 16, 2011

Science (print ISSN 0036-8075; online ISSN 1095-9203) is published weekly, except the last week in December, by the American Association for the Advancement of Science, 1200 New York Avenue NW, Washington, DC 20005. Copyright 2011 by the American Association for the Advancement of Science; all rights reserved. The title *Science* is a registered trademark of AAAS.

References and Notes

1. W. Cai, V. Shalaev, *Optical Metamaterials: Fundamentals and Applications* (Springer, New York, 2010).
2. D. R. Smith, J. B. Pendry, M. C. K. Wiltshire, *Science* **305**, 788 (2004).
3. N. Engheta, R. W. Ziolkowski, *Metamaterials, Physics and Engineering Explorations* (IEEE-Wiley, New York, 2006).
4. G. V. Eleftheriades, K. G. Balmain, *Negative-Refraction Metamaterials* (IEEE, New York, 2005).
5. J. B. Pendry, D. Schurig, D. R. Smith, *Science* **312**, 1780 (2006).
6. D. Schurig *et al.*, *Science* **314**, 977 (2006).
7. U. Leonhardt, *Science* **312**, 1777 (2006).
8. S. Maier, *Plasmonics: Fundamentals and Applications* (Springer, New York, 2007).
9. K. S. Novoselov *et al.*, *Nature* **438**, 197 (2005).
10. A. K. Geim, K. S. Novoselov, *Nat. Mater.* **6**, 183 (2007).
11. D. R. Anderson, *J. Opt. Soc. Am. B* **27**, 818 (2010).
12. F. Rana, *IEEE Trans. NanoTechnol.* **7**, 91 (2008).
13. E. G. Mishchenko, A. V. Shytov, P. G. Silvestrov, *Phys. Rev. Lett.* **104**, 156806 (2010).
14. V. V. Cheianov, V. Fal'ko, B. L. Altshuler, *Science* **315**, 1252 (2007).
15. P. R. West *et al.*, *Laser Photon. Rev.* **4**, 795 (2010).
16. N. Papasimakis *et al.*, *Opt. Express* **18**, 8353 (2010).
17. V. P. Gusynin, S. G. Sharapov, J. P. Carbotte, *J. Phys. Condens. Matter* **19**, 026222 (2007).
18. Z. Q. Li *et al.*, *Nat. Phys.* **4**, 532 (2008).
19. Materials and methods are available as supporting material on *Science* Online.
20. G. W. Hanson, *J. Appl. Phys.* **103**, 064302 (2008).
21. S. A. Mikhailov, K. Ziegler, *Phys. Rev. Lett.* **99**, 016803 (2007).
22. M. Jablan, H. Buljan, M. Soljacic, *Phys. Rev. B* **80**, 245435 (2009).
23. E. H. Hwang, S. D. Sarma, *Phys. Rev. B* **75**, 205418 (2007).
24. For example, for a layer of graphene free standing in air at $T = 3$ K with $\Gamma = 0.43$ meV and $\mu_c = 0.15$ eV at frequency 30 THz, $\mathrm{Re}(\beta) = 69.34k_0$ and $\mathrm{Im}(\beta) = 0.71k_0$. The corresponding numbers for the SPP at the air-silver interface in the mid IR wavelengths are approximately $\mathrm{Re}(\beta) \approx k_0$ and $\mathrm{Im}(\beta) < 10^{-4}k_0$, resulting in a very weakly confined SPP.
25. R. Dehbashi, D. Fathi, S. Mohajerzadeh, B. Forouzandeh, *IEEE J. Sel. Top. Quantum Electron.* **16**, 394 (2010).
26. The formation of such highly confined SPP is not due to direct interaction of light with the ground plane because obviously the confined SPP still exists for a free-standing graphene. The SPP wave is so highly confined that its field does not even "touch" the ground plane underneath. Therefore, without loss of generality, in all of our numerical studies the simulations are performed for the free-standing graphene in vacuum and with no ground plane present.
27. N. Engheta, *Science* **317**, 1698 (2007).
28. A. Alu, N. Engheta, *Phys. Rev. B* **75**, 024304 (2007).
29. T. Zentgraf, Y. Liu, M. H. Mikkelsen, J. Valentine, X. Zhang, *Nat. Nanotechnol.* **6**, 151 (2011).
30. P. A. Huidobro, M. L. Nesterov, L. Martín-Moreno, F. J. García-Vidal, *Nano Lett.* **10**, 1985 (2010).

Acknowledgments: This work is supported in part by the U.S. Air Force Office of Scientific Research (AFOSR) grants FA9550-08-1-0220 and FA9550-10-1-0408. Authors have no conflict of interest. A provisional patent application on the ideas presented in this manuscript has been filed by the University of Pennsylvania.

Supporting Online Material
www.sciencemag.org/cgi/content/full/332/6035/1291/DC1
Materials and Methods
SOM Text
Figs. S1 to S9
References

10 January 2011; accepted 11 April 2011
10.1126/science.1202691

Wafer-Scale Graphene Integrated Circuit

Yu-Ming Lin,* Alberto Valdes-Garcia, Shu-Jen Han, Damon B. Farmer, Inanc Meric,† Yanning Sun, Yanqing Wu, Christos Dimitrakopoulos, Alfred Grill, Phaedon Avouris,* Keith A. Jenkins

A wafer-scale graphene circuit was demonstrated in which all circuit components, including graphene field-effect transistor and inductors, were monolithically integrated on a single silicon carbide wafer. The integrated circuit operates as a broadband radio-frequency mixer at frequencies up to 10 gigahertz. These graphene circuits exhibit outstanding thermal stability with little reduction in performance (less than 1 decibel) between 300 and 400 kelvin. These results open up possibilities of achieving practical graphene technology with more complex functionality and performance.

Graphene, a layer of carbon atoms arranged in a hexagonal lattice, is a promising candidate for future high-speed electronics and radio-frequency (RF) applications (*1–4*) because of its high carrier mobility and saturation velocity (*5*). The planar structure and the feasibility of large-area graphene synthesis facilitate the adoption of top-down device fabrication techniques. Graphene transistors with intrinsic cut-off frequencies beyond 100 GHz have been recently achieved by several groups using graphene films synthesized by various methods, including epitaxial growth on SiC (*6*, *7*), chemical vapor deposition (CVD) on Cu (*8*), and mechanical exfoliation (*9*, *10*). The monolithic integration of transistors with interconnects and other components is an essential requirement for any semiconductor material to achieve a widespread technological impact. Previous attempts to make circuits based on graphene have used an indi-

IBM Thomas J. Watson Research Center, Yorktown Heights, NY 10598, USA.

*To whom correspondence should be addressed. E-mail: yming@us.ibm.com (Y.-M.L.); avouris@us.ibm.com (P.A.)
†Present address: Columbia University, New York, NY 10027, USA.

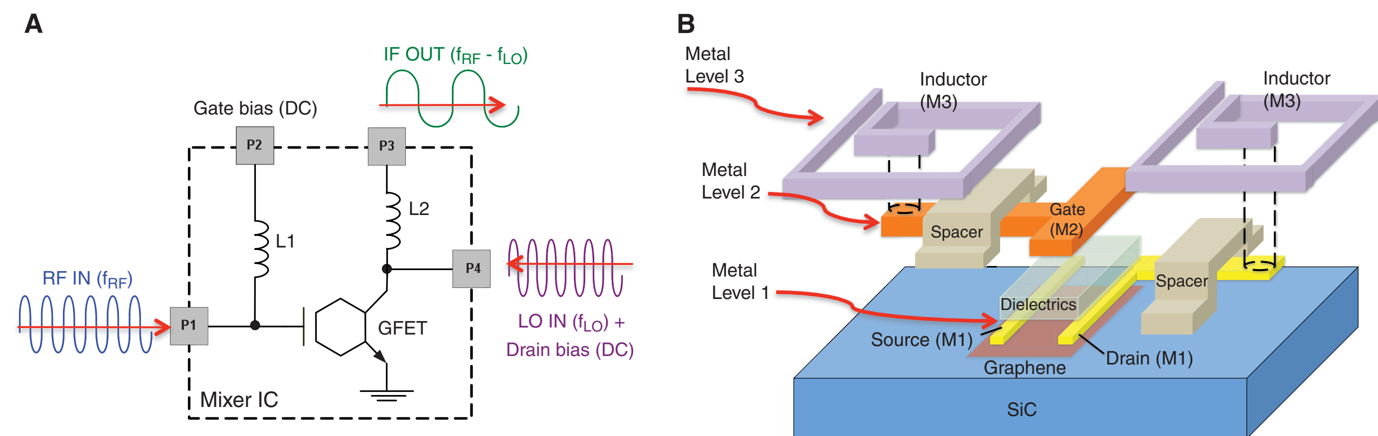

Fig. 1. (**A**) Circuit diagram of a four-port graphene RF frequency mixer. The scope of the graphene IC is confined by the dashed box. The hexagonal shape represents a graphene FET. (**B**) Schematic exploded illustration of a graphene mixer circuit. The critical design aspects include a top-gated graphene transistor and two inductors connected to the gate and the drain of the GFET. Three distinct metals layers of the graphene IC are represented by M1, M2, and M3. A layer of 120-nm-thick SiO_2 is used as the isolation spacer to electrically separate the inductors (M3) from the underlying interconnects (M1 and M2).

Downloaded from www.sciencemag.org on June 16, 2011

vidual graphene transistor connected to external passive elements (*11–13*). Such heterogeneous circuitry inevitably results in degraded performance dominated by interconnects and parasitics rather than the intrinsic properties of graphene device. For example, Wang *et al.* demonstrated an RF frequency mixer operating at a few tens of megahertz based on a single graphene transistor (*12*).

Despite recent progress in graphene synthesis and device performance, scalable integration of graphene into a practical circuit remains challenging. The key difficulties stem from the distinct materials properties of graphene with respect to those of conventional semiconductors, such as a different ohmic contact formation mechanism (*14*), poor adhesion with metals and oxides (*15*, *16*), and its vulnerability to damage in plasma processing. Thus, bridging the technological gap between a single device and a practical graphene circuit on the wafer scale requires innovative integration processes and circuit designs. Here, we describe wafer-scalable processes that have been developed to fabricate arrays of graphene analog circuits, each consisting of one graphene transistor and two inductors, all compactly integrated on a single SiC substrate. The entire integrated circuit (IC), including the contact pads, is less than 1 mm^2, and successful integration is verified by operating it as an RF mixer at a designated gigahertz frequency range.

The previously demonstrated frequency multipliers and mixers using graphene field-effect transistors (GFETs) were based on the ambipolar transport characteristics of CVD and exfoliated graphene (*11–13*). The mixer circuit design exploits a general gate-driven and drain-driven current modulation behavior in GFETs that can be used in both ambipolar and unipolar devices. Mixers are electrical circuits used for frequency conversion and are critical components in modern RF communication systems. Two high-frequency signals, an RF signal at a frequency f_{RF} and a local oscillator (LO) signal at a frequency f_{LO}, are applied to the gate and the drain of the GFET through port P1 and port P4, respectively (Fig. 1A). The graphene transistor is modulated by both signals and produces a drain current that contains the mixed frequencies, the sum ($f_{RF} + f_{LO}$), and the difference ($f_{RF} - f_{LO}$, the intermediate frequency f_{IF}) of the input frequencies. The integrated inductors complement the graphene FET to form an integrated RF mixer. Inductor L1 resonates out the parasitic capacitances from the input RF pad and the gate of the graphene FET, while inductor L2 provides an input match to the LO signal and acts as a low-pass filter between the drain of the FET and the output port P3. In practice (e.g., in a radio receiver application), frequencies of the RF and LO input signals differ by only a small amount, and the output signal component of interest is f_{IF}.

Graphene circuits were fabricated on a semi-insulating SiC wafer. A two- or three-layer graphene film was epitaxially grown on the Si face of the SiC substrate at temperatures above 1400°C (*17–19*), as confirmed by Raman spectroscopy and optical absorption measurements (see fig. S1 in the supporting online material). Fabrication of the graphene IC began with top-gated, two-finger graphene FETs (Fig. 2A), followed by integration with on-chip inductors. To form the active channel of the transistor, we spin-coated the graphene-SiC wafer with a layer of 140-nm-thick PMMA [poly(methyl methacrylate)] followed by a layer of 20-nm-thick HSQ (hydrogen silsesquioxane). The FET channel was defined by e-beam lithography (EBL); the surrounding graphene was removed by an oxygen plasma with the exposed HSQ film as the protecting mask. The HSQ-PMMA stack over the channel region was subsequently removed by acetone.

The removal of graphene film on SiC outside of the active channel region was critical to achieve good adhesion of thick metals in the subsequent deposition processes. The ohmic source and drain contacts, contact pads, and gate electrode were all made of the same metal stack of 20-nm Pd, 40-nm Au. The gate length was 550 nm and the distance between source and drain contacts was 600 nm. The gate dielectric was deposited by evaporating two 2-nm layers of Al metal onto the graphene channel that were then oxidized at elevated temperatures (~ 120°C) in air to form a seed layer for the subsequent deposition of Al_2O_3 (20 nm) by atomic layer deposition (*14*). The capacitance of the resulting gate dielectric stack was ~2. 5 × 10^{-7} F/cm^2.

Inductors were defined by EBL and formed by depositing 1-μm-thick Al metal. A layer of 120-nm-thick SiO_2, deposited by e-beam evaporation, was used to isolate the inductor loops from the underlying metal interconnects. The inductor had a value of 5.2 nH, a self-resonant frequency of ~10 GHz, and quality factor (Q) of 5, as measured on a stand-alone test site. The inductance was designed to achieve a target operation frequency of 5 GHz for the mixer circuit, and the quality factor of 5 is appropriate for broadband

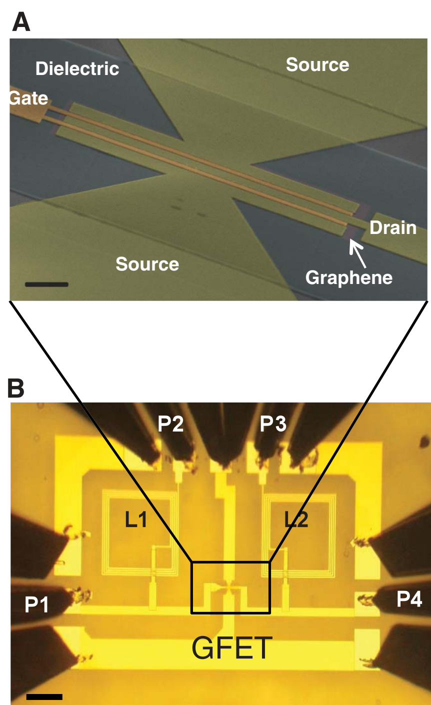

Fig. 2. Images of graphene ICs. (**A**) Scanning electron image of a top-gated, dual-channel graphene transistor used in the mixer IC. The gate length is 550 nm and the total channel width, including both channels, is 30 μm. Scale bar, 2 μm. (**B**) Optical image of a completed graphene mixer including contact pads. The gound-signal-ground configuration is implemented for the probe pads suitable for direct RF testing. Scale bar, 100 μm.

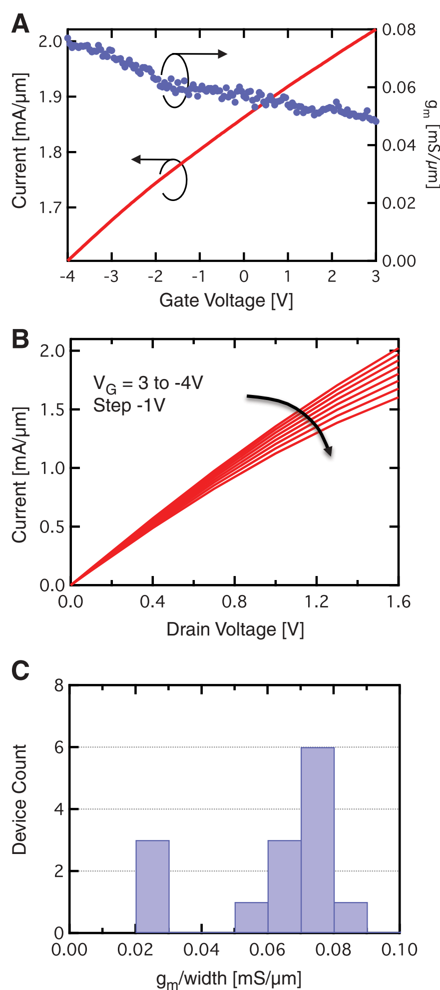

Fig. 3. (**A**) The drain current I_d of a 550-nm–gate-length graphene FET as a function of gate voltage V_g at a drain bias of 1.6 V with the source electrode grounded. The current shown was normalized with respect to the total channel width. The device conductance g_m is shown on the right axis. (**B**) The measured drain current I_d as a function of drain bias of the graphene FET for various top-gate voltages. (**C**) Distribution of peak g_m of graphene FETs, all of the same gate length of 550 nm and fabricated on the same wafer.

Downloaded from www.sciencemag.org on June 16, 2011

operation. Figure 2B shows an image of the completed graphene circuit, including the inductors, GFET, and contact pads. The layout of the entire die, containing arrays of graphene ICs used as monitor devices and other testing components, is shown in fig. S3.

Figure 3A shows the current I_d and transconductance g_m as a function of gate voltage V_g of a typical graphene transistor with a gate length of 550 nm at drain voltage V_d = 1.6 V measured at room temperature. Within the gate voltage range studied here, the GFETs always exhibited dominant n-type transport (*6*, *17*, *19*), which differs from the ambipolar characteristics typically observed in CVD and exfoliated graphene. The output characteristics of the GFET (Fig. 3B) exhibited a nearly linear I_d-V_d dependence for all gate voltages up to a drain voltage of 1.6 V. These triode-like output characteristics resulted in a device transconductance that increased with rising V_d. At a drain bias of 1.6 V, a current density above 2 mA/µm and a transconductance of 80 µS/µm were achieved. The measured current density was enhanced by the high intrinsic doping level (up to 10^{13} cm^{-2}) of graphene. Figure 3C shows the distribution of the peak transconductance of 13 GFETs fabricated on the same wafer, with most devices ranging between 60 and 80 µS/µm. The contact resistance of the graphene transistor, which included the source and drain contacts, was about 600 ohm·µm. On the basis of the measured dc transconductance and gate capacitance, the intrinsic cut-off frequency of the GFET is estimated to be ~9 GHz for a gate length of 550 nm and drain bias of 1.6 V.

Unlike conventional mixers that are typically realized by applying LO and RF signals to a nonlinear device, such as a Schottky-barrier diode, the mixer IC discussed here uses channel resistance modulation of the graphene FET to achieve frequency mixing. The drain current exhibits a nearly linear dependence with respect to gate and drain voltages (Fig. 3, A and B) and can be expressed, to the first-order approximation, by $I_d \approx A \cdot (B + g_m \cdot V_g) \cdot V_d$, where A and B are constants. The frequency mixing becomes evident in view of the product term of V_g and V_d. Because the output signal is proportional to the drain current modulation, the power of output signal f_{IF} is proportional to the product of the transconductance $g_m = \left(\frac{dI_d}{dV_g}\right)$ and the output conductance $g_d = \left(\frac{dI_d}{dV_d}\right)$. Although current saturation in the I_d-V_d curves, which corresponding to a small g_d, is a desirable feature for RF and analog applications in general, it remains challenging to achieve well-behaved current saturation in graphene FETs, especially for small gate lengths (*20*, *21*). Most graphene devices exhibit a triode-like I_d-V_d behavior such as the one shown in Fig. 3B. By using the finite conductance g_d of graphene transistors to realize mixing, the output signal is linearly proportional to both gate and drain input signals. This configuration has been previously used with GaAs FETs operating in the linear region (*22*), achieving a superior linearity compared to mixers that use diodes or FETs operating in saturation mode.

Figure 4A displays the output frequency spectrum of the graphene mixer with input signals f_{RF} = 3.8 GHz and f_{LO} = 4 GHz and a drain bias of 2 V. The frequency mixing function was visible as two tones observed at frequencies f_{IF} of 200 MHz and $f_{RF} + f_{LO}$ of 7.8 GHz. The higher-frequency tone was attenuated by the drain inductor and hence showed lower amplitude. The power of signal f_{IF} was proportional to that of the input RF signal up to P_{RF} = 12 dBm for an LO signal as high as P_{LO} = 20 dBm (fig. S5); this high level of linearity is expected from the mixer configuration as described above. The conversion loss, defined as the power ratio of the IF signal P_{IF} and the input RF signal P_{RF}, is about −27 dB. Figure 4B shows the dependence of conversion loss of the mixer on the LO frequency while maintaining f_{IF} at 200 MHz. The performance of this graphene mixer peaked around f_{LO} ~ 4.5 GHz, which is in good agreement with the target frequency of 5 GHz. These results not only validate the proper function of the graphene circuit as an RF mixer, but also demonstrate successful integration and operation of an active graphene device coupled with supporting components on a single chip.

Figure 4C shows the dependence of conversion loss of the mixer on dc gate voltage, revealing a trend that qualitatively follows the variation of transconductance g_m as a function of V_g (Fig. 3A). The strong correlation between the conversion loss and g_m shows that performance of the graphene mixer was determined by the properties of GFET itself and not by parasitic signal transmission. The conversion gain can be enhanced by further improving g_m, e.g., by adopting a thinner oxide and a shorter channel length. As the drain voltage increases from 0.3 to 2 V, the conversion loss is improved by about +3 dB, in agreement with the increasing g_m with V_d (Fig. 3B). The conversion loss of all mixers fabricated on the same wafer and measured at identical dc bias conditions varied within ±2 dB (Fig. 4D). To evaluate temperature response of these graphene ICs, we measured the mixer performance as a function of temperature up to T = 400 K. In conventional semiconductor devices, the performance is usually severely degraded as T increases, and additional feedback circuitry is required to minimize the thermal sensitivity. In contrast, the con-

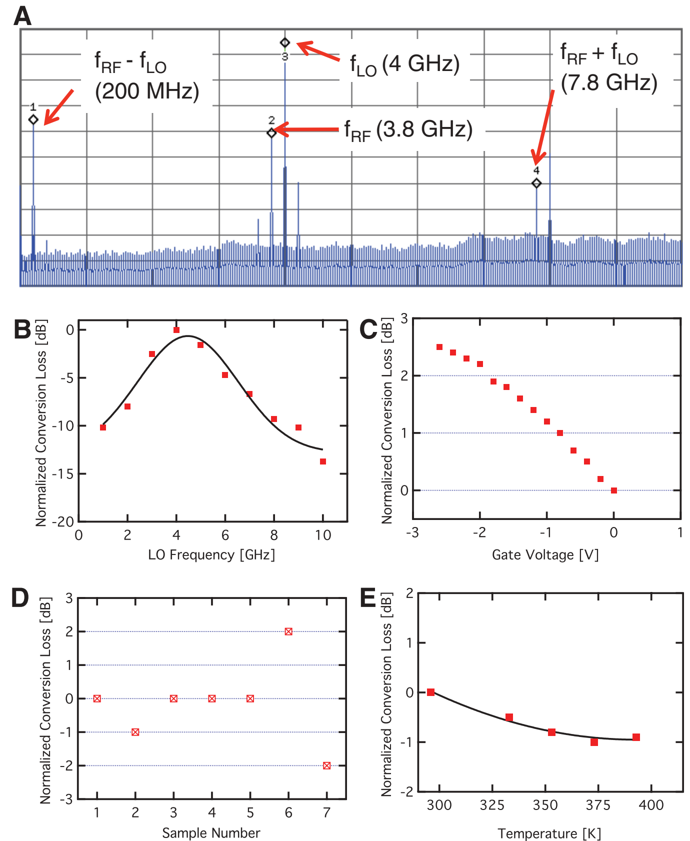

Fig. 4. (**A**) A snapshot of output spectrum, between 0 and 10 GHz, of the mixer taken from the spectrum analyzer with f_{RF} = 3.8 GHz and f_{LO} = 4 GHz. Each x and y division corresponds to 1 GHz and 10 dBm, respectively. The graphene FET was biased at a drain bias of 2 V and a gate voltage of −2 V. The input RF power was adjusted to 0 dBm, so that the output spectrum power measured the actual loss (gain) with respect to the RF input. The frequency mixing was visible with two peaks observed at frequencies of 200 MHz and 7.8 GHz with signal power of −27 and −52 dBm, respectively. (**B**) Measured conversion loss of the graphene frequency mixer as a function of LO frequency. The conversion loss was normalized to the value at f_{LO} = 4 GHz. The solid line is a guide to the eye. (**C**) Conversion loss of the mixer measured as a function of V_g of the graphene FET, normalized to the value at V_g = −3 V. (**D**) Distribution of the conversion loss of seven working graphene mixer ICs, all fabricated on the same wafer. The conversion loss was normalized to their average value. (**E**) Temperature dependence of conversion loss of the graphene mixer between 300 and 400 K measured at V_d = 1 V and V_g = −1 V. The conversion loss was normalized to the value at 300 K, showing performance degradation less than 1 dB in this temperature range. The solid line is a guide to the eye.

Downloaded from www.sciencemag.org on June 16, 2011

version loss of the graphene mixer exhibits little, if any, temperature dependence with a variation below 1 dB in this wide range from 300 to 400 K (Fig. 4E). The absence of strong temperature dependence of graphene ICs is attributed to a degenerate doping level in these GFETs and a nearly *T*-independent scattering mechanism associated with optical phonons at high biases (*8*, *20*, *23*).

The integration techniques and operating principles of graphene circuits described here can be applied to CVD graphene and are also compatible with optical lithography for reduced cost and enhanced throughput. The fabricated graphene IC achieved a 27-dB conversion loss at 4 GHz. In comparison, previously reported graphene-based mixers operated at 10 MHz with a 40-dB conversion loss (*14*), and a commercially available GaAs-based mixer achieves 7-dB conversion loss at 1.95 GHz (*24*). In addition, the operation of these mixers required external passive components, whereas the graphene mixer presented here was integrated. The use of thin high-*k* dielectrics (e.g., 2 nm HfO_2) or highly scaled gate lengths (e.g., 40 nm) (*8*) could improve the FET transconductance by a factor of 10, which would lead to an enhancement of more than 20 dB in conversion gain for the graphene mixer. Moreover, such FET improvement in combination with the integration scheme described here would also enable other graphene-based circuits, such as amplifiers and oscillators, and their use in wireless communication systems.

References and Notes

1. A. K. Geim, K. S. Novoselov, *Nat. Mater.* **6**, 183 (2007).
2. Y. B. Zhang, Y. W. Tan, H. L. Stormer, P. Kim, *Nature* **438**, 201 (2005).
3. C. Berger *et al.*, *Science* **312**, 1191 (2006).
4. P. Avouris, *Nano Lett.* **10**, 4285 (2010).
5. K. Bolotin *et al.*, *Solid State Commun.* **146**, 351 (2008).
6. Y.-M. Lin *et al.*, *Science* **327**, 662 (2010).
7. J. S. Moon *et al.*, *IEEE Electron Device Lett.* **31**, 260 (2010).
8. Y. Wu *et al.*, *Nature* **472**, 74 (2011).
9. Y.-M. Lin *et al.*, *Nano Lett.* **9**, 422 (2009).
10. L. Liao *et al.*, *Nature* **467**, 305 (2010).
11. H. Wang, D. Nezich, J. Kong, T. Palacios, *IEEE Electron Device Lett.* **30**, 547 (2009).
12. H. Wang, A. Hsu, J. Wu, J. Kong, T. Palacios, *IEEE Electron Device Lett.* **31**, 906 (2010).
13. X. Yang, G. Liu, A. A. Balandin, K. Mohanram, *ACS Nano* **4**, 5532 (2010).
14. F. Xia, V. Perebeinos, Y.-M. Lin, Y. Wu, P. Avouris, *Nat. Nanotechnol.* **6**, 179 (2011).
15. S. Kim *et al.*, *Appl. Phys. Lett.* **94**, 062107 (2009).
16. Q. H. Wang, M. C. Hersam, *Nat. Chem.* **1**, 206 (2009).
17. C. Dimitrakopoulos *et al.*, *J. Vac. Sci. Technol. B* **28**, 985 (2010).
18. D. K. Gaskill *et al.*, *ECS Trans.* **19**, 117 (2009).
19. K. V. Emtsev *et al.*, *Nat. Mater.* **8**, 203 (2009).
20. I. Meric *et al.*, *Nat. Nanotechnol.* **3**, 654 (2008).
21. C. R. Dean *et al.*, *Nat. Nanotechnol.* **5**, 722 (2010).
22. S. A. Maas, *IEEE Trans. Microw. Theory Tech.* **35**, 425 (1987).
23. V. Perebeinos, P. Avouris, *Phys. Rev. B* **81**, 195442 (2010).
24. ADL5350 from Analog Devices; the datasheet is available at www.analog.com/static/imported-files/data_sheets/ADL5350.pdf

Acknowledgments: We are grateful to B. Ek and J. Bucchignano for technical assistance and to D. K. Gaskill for providing some epitaxial graphene wafers for testing. We also acknowledge discussions with F. Xia, T. Mcardle, H.-Y. Chiu, and C. Y. Sung. We thank Defense Advanced Research Projects Agency (DARPA) for financial support through the CERA program (contract FA8650-08-C-7838). The views, opinions, and/or findings contained here are those of the authors and do not represent the official views or policies of DARPA or the Department of Defense.

Supporting Online Material
www.sciencemag.org/cgi/content/full/332/6035/1294/DC1
Materials and Methods
Figs. S1 to S6
References

16 February 2011; accepted 22 April 2011
10.1126/science.1204428

Downloaded from www.sciencemag.org on June 16, 2011

Endotoxin-Induced Structural Transformations in Liquid Crystalline Droplets

I-Hsin Lin,[1] Daniel S. Miller,[1] Paul J. Bertics,[2] Christopher J. Murphy,[3,4] Juan J. de Pablo,[1] Nicholas L. Abbott[1]*

The ordering of liquid crystals (LCs) is known to be influenced by surfaces and contaminants. Here, we report that picogram per milliliter concentrations of endotoxin in water trigger ordering transitions in micrometer-size LC droplets. The ordering transitions, which occur at surface concentrations of endotoxin that are less than 10^{-5} Langmuir, are not due to adsorbate-induced changes in the interfacial energy of the LC. The sensitivity of the LC to endotoxin was measured to change by six orders of magnitude with the geometry of the LC (droplet versus slab), supporting the hypothesis that interactions of endotoxin with topological defects in the LC mediate the response of the droplets. The LC ordering transitions depend strongly on glycophospholipid structure and provide new designs for responsive soft matter.

The functional properties of inorganic and organic materials have been manipulated through the deliberate introduction of defects and grain boundaries, as well as through the partitioning of low concentrations of dopant species to these localized regions of the materials (*1*–*4*). For soft materials, such as liquid crystals (LCs), geometrical confinement within micrometer-sized systems has been shown to lead to the formation of a range of thermodynamically stable defects with nanoscopic dimensions and varied topologies (points, lines, rings) (*5*–*11*). In this paper, we report that confinement of LCs within micrometer-sized droplets dispersed in water can lead to ordering transitions in the LC droplets that are highly specific and sensitive to a particular bacterial glycophospholipid. These ordering transitions occur at concentrations of lipid that are six orders of magnitude lower than previously reported adsorbate-driven ordering transitions in LC systems (*10*–*13*).

[1]Department of Chemical and Biological Engineering, University of Wisconsin–Madison, 1415 Engineering Drive, Madison, WI 53706–1607, USA. [2]Department of Biomolecular Chemistry, University of Wisconsin–Madison, 1300 University Avenue, Madison, WI 53706–1510, USA. [3]Department of Ophthalmology and Vision Science, School of Medicine, University of California, Davis, CA 95616, USA. [4]Department of Veterinary Surgical and Radiological Sciences, School of Veterinary Medicine, University of California, Davis, CA 95616, USA.

*To whom correspondence should be addressed. E-mail: abbott@engr.wisc.edu

Endotoxin is a bacterial lipopolysaccharide comprised of a glycophospholipid (called lipid A) (Fig. 1A) in addition to two polysaccharide domains. Lipid A has six tails, and thus it is structurally distinct from all other lipids (*14*). We investigated the interactions of endotoxin from *Escherichia coli*, the lipid A portion of endotoxin, and the other phospholipids and surfactants shown in Fig. 1, B to D, with micrometer-sized droplets of nematic LC [4′-pentyl-4-cyanobiphenyl (5CB)] (Fig. 1E) that were dispersed initially in endotoxin-free water (*15*). In the absence of endotoxin, bright-field (Fig. 1F) and polarized light micrographs (Fig. 1G) revealed the presence of two point defects (surface defects, called boojums) located at the "poles" of the LC droplets, corresponding to a so-called bipolar configuration of the droplet where the LC assumes a tangential orientation at the droplet surface (Fig. 1H) (*5*). After the addition of endotoxin to the water at a concentration of 1 μg/ml, both bright-field (Fig. 1I) and polarized light imaging (Fig. 1J) revealed a reordering of the LC within the droplet to a so-called radial configuration, corresponding to a single defect located at the droplet center and LC oriented perpendicular to the droplet surface (Fig. 1K) (*5*). Upon measuring the fraction of LC droplets within a solution of endotoxin that exhibited the radial configuration (Fig. 1L), we found that remarkably low concentrations of endotoxin (<1 pg/ml) trigger the ordering transition. Consistent with our conclusion that the interaction of the LC droplets and endotoxin was responsible for the ordering transition, the fraction of LC droplets in the radial configuration increased with the concentration of endotoxin (Fig. 1L). The response of the LC